Smart Materials and Structures

PURPOSE-LED PUBLISHING™

**PAPER** • **OPEN ACCESS**

# Investigation of scalable chiral metamaterial beams for combined stiffness and supplemental energy dissipation

To cite this article: Han Liu and Simon Laflamme 2024 *Smart Mater. Struct.* **33** 115051

OPEN ACCESS
IOP Publishing
Smart Materials and Structures
Smart Mater. Struct. **33** (2024) 115051 (19pp)
https://doi.org/10.1088/1361-665X/ad8a30

# Investigation of scalable chiral metamaterial beams for combined stiffness and supplemental energy dissipation

**Han Liu*** **and Simon Laflamme**

Department of Civil, Construction, and Environmental Engineering, Iowa State University, Ames, IA 50011, United States of America

E-mail: liuhan@iastate.edu

Received 2 May 2024, revised 17 August 2024
Accepted for publication 22 October 2024
Published 1 November 2024

**Abstract**

Metamaterials have gained important interest in the research community attributable to advances in additive manufacturing enabling their fabrication at reasonable costs. The vast majority of their applications and demonstrations are at micro- and nano-scales, and challenges remained regarding the larger scale applications. In this paper, we are interested by the scalability of metamaterials, targeting structural engineering applications. To do so, we explore mechanisms capable of providing both bending stiffness and high-performance energy dissipation. Our study includes beams constructed with chiral topologies of different structural hierarchy orders, and we also explore three new topologies that we termed chiral friction, chiral-rectangular and chiral-hexagonal design to engineer the beams and the use of friction rods with tunable post-stress that inserted longitudinally through the beams to provide enhanced friction. The mechanical performance of the metamaterial beams is characterized through a series three-point bending tests. Of interest is to evaluate the bending stiffness, shape recoverability, and energy dissipation capabilities. We find that the chiral-hexagonal topology equipped with a non-stressed friction rod exhibit excellent energy dissipation capabilities, showing an improved loss factor by 11.9 times compared to the control beam using 68% of its materials density. Moreover, the use of the post-stress mechanism shows that it is possible to augment both its shape recovery and bending stiffness up to 99.3% and 47.1%, respectively. Overall, our investigation shows that it is possible to engineer scalable metamaterial beams targeting structural engineering applications, and that the use of topology optimization and strategically designed post-tensioning mechanism can allow tuning of mechanical performance.

Keywords: metamaterial, chiral, friction, energy dissipation, stiffness, additive manufacturing

## 1. Introduction

Metamaterials, also known as programmable materials or lattices, are man-made or artificially engineered materials whose characteristics predominantly stem from the deliberate design of their topologies [1]. Metamaterials have gained important popularity in the engineering community in recent years because they enable the manipulation and control of materials properties in ways that are not naturally occurring. These materials may exhibit exceptional properties and performance beyond those of conventional materials, including negative Poisson's ratio, mechanical bi-stability, and ultra-high damping [2, 3]. They have also sparked significant interest

* Author to whom any correspondence should be addressed.

in photonics and optoelectronics [4] due to their negative refraction and cloaking properties [5], and found applications in vibroacoustics and phononics for the development of acoustic lenses, sound barriers, and vibration isolation systems [6, 7].

The vast majority of work on metamaterials has been conducted on micro- and nano-scales structures. Of interest to this paper is the macro-scale targeting applications to structural engineering, where applications and demonstrations have been largely overlooked [8]. Metamaterials can have important benefits for the structural engineering community as they could be used to substantially enhance structural resilience and sustainability. In particular, they can provide supplemental damping while minimizing the use of materials through strategic topological designs [9]. The lack of research on scalable metamaterials can be attributed to the high cost and difficulty in fabricating larger components of complex geometries [10]. Recent advance and breakthroughs in additive manufacturing have offer unprecedented freedom to design and empower engineers with the capability to 3D print large components much faster and cheaper than ever done before. Such advances are partly responsible for the popularity of metamaterials amongst researchers by bridging the gap between materials design and applications, and are now making the fabrication of large-scale metamaterials a reality [11, 12].

Lattice-type metamaterials derive their unique properties and unusual deformation from the deliberate design of their lattice-like structures [13, 14]. Incorporating lattice configurations within metamaterial can confer remarkable mechanical properties and novel multifunctionalities, such as high stiffness, tunable vibroacoustic properties, enhanced energy absorption, and shape recoverability [15–18], partly attributable to their anisotropic and non-reciprocal responses [19, 20]. For example, lattice topologies have been shown to exhibit a notable ability to recover from compressive deflection while dissipating significant amounts of energy through mechanisms such as local beam buckling, friction, plastic deformation, and intrinsic material damping [21–23]. This is particularly noteworthy as even materials like ceramics and metals, which typically lack intrinsic reversible energy dissipation, can be engineered or architected with lattice topologies to impart dissipation properties akin to elastomers [24]. However, some lattice struts within the typical lattice topologies are designed to attenuate and dissipate mechanical energy through the plastic deformation and fracture of the structural component, thereby making the energy dissipation process irreversible [25–29]. A prevalent solution involves combining lattice and chiral topologies to increase buckling stability and potentially creating sliding friction and relatively low densities. These lightweight lattice structures offer the possibility of repeatable energy dissipation beyond the range of traditional viscoelastic materials and are well-suited for protective applications requiring controlled energy dissipation at controlled loading levels [30, 31].

The chiral structure/topology is a set of arrangements that cannot be transformed into their mirrored images solely through rotations and translations [19]. These structure are typically constructed by connecting ribs tangentially to cylindrical or quadratic units [32, 33] and can be found commonly in nature, including DNA, RNA, twisting flower petals, and plant climbing tendrils [34–36]. Chirality in metamaterials topologies adds another layer of capability, particularly in applications where directionality and selective filtering of waves are crucial. For example, chiral structures have been employed in the metamaterials design of advanced acoustic devices that exhibit directional sound propagation, enabling precise control over sound waves for noise reduction and sound steering applications [37, 38]. In the field of phononics, chiral metamaterials have been used to create materials with tailored band gaps that allow for the selective transmission of mechanical waves, useful in creating nonreciprocal wave propagation, acoustic cloaking, and energy harvesting systems [39]. In engineering, these microstructural design confer materials with multifunctional properties such as vibration attenuation, impact energy absorption, and negative thermal expansion [40–42]. Chiral lattice metamaterials with different structural hierarchy orders have been proposed and fabricated to dissipate energy via stick-slip friction, intrinsic material damping (i.e. viscoelasticity effect), and surface interaction [43, 44]. Findings from published literature suggest the possibility of manufacturing lightweight and high-energy dissipation metamaterials at large scale.

Targeting structural engineering applications, we investigated in this paper the use of scalable chiral lattice metamaterial designs to achieve superior energy dissipation under external loads while maintaining appropriate bending stiffness. In general, these two objectives, energy dissipation and stiffness, can be conflicting, because structural damping increases with structural motion [45]. A novel approach proposed in this paper is to integrate post-stressable friction rods in some of the specimens to study the capability to manipulate stiffness, and study its effect on damping characteristics. Supplemental energy dissipation through sliding friction caused by external elements have been studied in [1], where the authors investigated damping characteristics of interpenetrating lattices. Here, our friction bar is much simpler in topology, but includes the post-stress capability (using screw nuts) to attain a requisite stiffness.

We studied chiral lattice metamaterials with three orders of structural hierarchy ($N_1$, $N_2$, and $N_3$) that demonstrated repeatable energy dissipation effects in [44]. These chiral topologies were modified by adding wedge-shaped and V-shaped triangular elements at the slits to produce friction elements and thus create Coulomb friction energy dissipation through sliding motion. We also explored different chiral topologies, including a new chiral friction, a new chiral-rectangular and a new chiral-hexagonal design. Additional frictional effect is introduced in the chiral beam specimen by integrating friction rods consisting of natural nylon threaded rods running longitudinally through the middle of the beams, providing bending stiffness tunability and additional damping through sliding friction. The focus of this work is to experimentally characterize and evaluate the bending behavior and the energy dissipation performance of various chiral truss beams for understanding the scalability of metamaterials

for structural engineering applications. Therefore, a series of loading-controlled dynamic tests were performed on each chiral beam specimen using a three-point bending setup, and the mechanical properties in terms of the bending stiffness, deflection, recoverability, energy absorption, energy dissipation, and loss factors under different maximum loading magnitudes as well as different post-stress levels were characterized and compared. To allow the study to focus on design strategies rather than the parametrization of a single design, our experimental approach follows that of [1], whereas the dynamic tests are restricted to a single harmonic, and the study of the frequency-dependent behavior is left to future work. We concluded the paper by discussing promising designs and a path to engineering the next generation of scalable metamaterials.

## 2. Metamaterial topologies

### 2.1. Metamaterial design and fabrication

The initial chiral topologies investigated in this study were adopted from [43] (figures 1(a)–(c)). These chiral topologies follow a rotational symmetry about the center and include slits to create a series of hinges that initiates deformation mechanisms within the lattice through the bending and rotating of the ribs. The width of the perforations in those topology is typically relatively small compared to the shortest length of the unit cell, thereby creating the chiral topology with low porosity. The elements used in designing the topologies and metamaterial beams are as follows:

- Chiral pattern - The chiral topologies were characterized by the side length of the unit cell $a_i$, thickness of the rib $b_i$, and width of the slit $t_i$, with the subscript $i$ representing the order levels of different aspect ratios of slit to ribs (see figure 1), with:

$$a_i = s_i \times (b_i + t_i) \tag{1}$$

  where $s_i$ is an even integer that determines the slit motifs. Based on the fabrication resolution, here governed by the 3D printer, the three chiral hinge unit cells were designed with $a_i = 25$ mm and $s_i = 6$, 10, and 14 mm to create the three orders of structural hierarchy (namely $N_1$, $N_2$, and $N_3$) with the rib thicknesses $b_i$ respectively of 3.54, 1.87, and 1.16 mm to maintain a constant slit width $t_i$ of 0.625 mm. The resulting representative unit cells of $N_1$, $N_2$, and $N_3$ are diagrammed in figures 1(a)–(c), respectively.
- Chiral friction element - Two types of friction elements, namely wedge-shaped and V-shaped triangular elements, were incorporated at the slits of each chiral unit hinge cell to create Coulomb friction through the sliding motion produced when the unit cell was subjected to transverse bending (bending moment along the $z$-axis illustrated by the curved arrows in figure 1(h)). The rib thicknesses $b_i$ were reduced across all three orders of structural hierarchies to accommodate the friction elements, and both the wedge-shaped and V-shaped friction elements have a triangular shape and were characterized by the opposite length $l$ and the acute angles $\theta$ formed by the opposite and hypotenuse sides. Figures 1(d)–(g) shows key geometries for the wedge-shaped friction elements integrated in $N_1$, and for the V-shaped friction elements incorporated in $N_1$, $N_2$, and $N_3$, respectively. Remark that values for $l$ and $\theta$ are dependent on the length of each rib on which the friction element is incorporated, where $l$ equal to the full (wedge-shape) or half (V-shape) length of each rib, and $\theta$ varies to maintain the width of slits $s_1$ to $s_4$ equal to that of the initial chiral topologies ($t_1$, $t_2$, and $t_3$) at 0.6215 mm.
  Three more novel chiral topologies adopting a similar chiral mechanism were investigated. Those topologies were primarily engineered to dissipate energy through bending in the transverse direction. Their overall geometry were equal to those of the representative chiral units cell defined above. To make the proposed chiral topologies comparable to the initial chiral topologies, the design of the three chiral topologies kept the edge length of the unit cell $a_8$, $a_9$, and $a_{10}$ consistent with $a_1$ to $a_7$ at 25 mm, the slit width $t_8$, $t_9$, and $t_{10}$ consistent with $t_1$ to $t_3$ and $s_1$ to $s_4$ at 0.6215 mm, and the rib thicknesses $b_8$, $b_9$, and $b_{10}$ consistent with $b_2$ at 1.87 mm. The interested reader may refer to tables A1–A10 of the appendix to find geometric values used in designing each chiral topology.
- Chiral $N_2$ friction (CF) - The CF topology was based on the chiral $N_2$ topology, but with U-shaped-like elements incorporated in the design on both the horizontal and vertical ribs after modifying their thicknesses to $b_8 = b_2 =$ 1.87 mm and remaining slit width $t_8$ to be the same as $t_1$ to $t_3$ and $s_1 = s_4 = 0.6215$ mm. Those U-shaped-like elements formed trapezoid slits in the middle of each rib with a bottom base $l_1 = 1.2$ mm, top base $l_2 = 0.4$ mm, and inclined angle $\theta_1 = 150°$, thus creating contact friction and sliding motion-induced Coulomb friction. The resulting topology is diagrammed in figure 2(a), with a 3D view illustrated in figure 2(b).
- Chiral-rectangular (CR) - The CR topology had a hexagonal unit cell that comprised a series of concentric rectangles. This design altered the spatial arrangement to accommodate a set of triangular elements positioned on the ribs. Those triangular elements served as friction elements by sliding over each other under a transverse bending motion, resulting in repeatable energy dissipation. That CR topology was characterized by the aspect ratio defined as the ratio of length to the width of the rectangular lattice that had successively decreasing side lengths and triangular elements towards the geometric center. An aspect ratio of 3, maximum rectangular side length $l_3 = 20$ mm, maximum triangular side length $l_4$ of 5 mm, inclined angle $\theta_3 = 130°$, and number of hexagonal lattice of 3 were taken to defined the CR topology. A rib width $b_9$ and slit width $t_9$ were taken as equal to those from the $N_2$ friction topology. The resulting topology is diagrammed in figure 2(c), with a 3D view illustrated in figure 2(d).

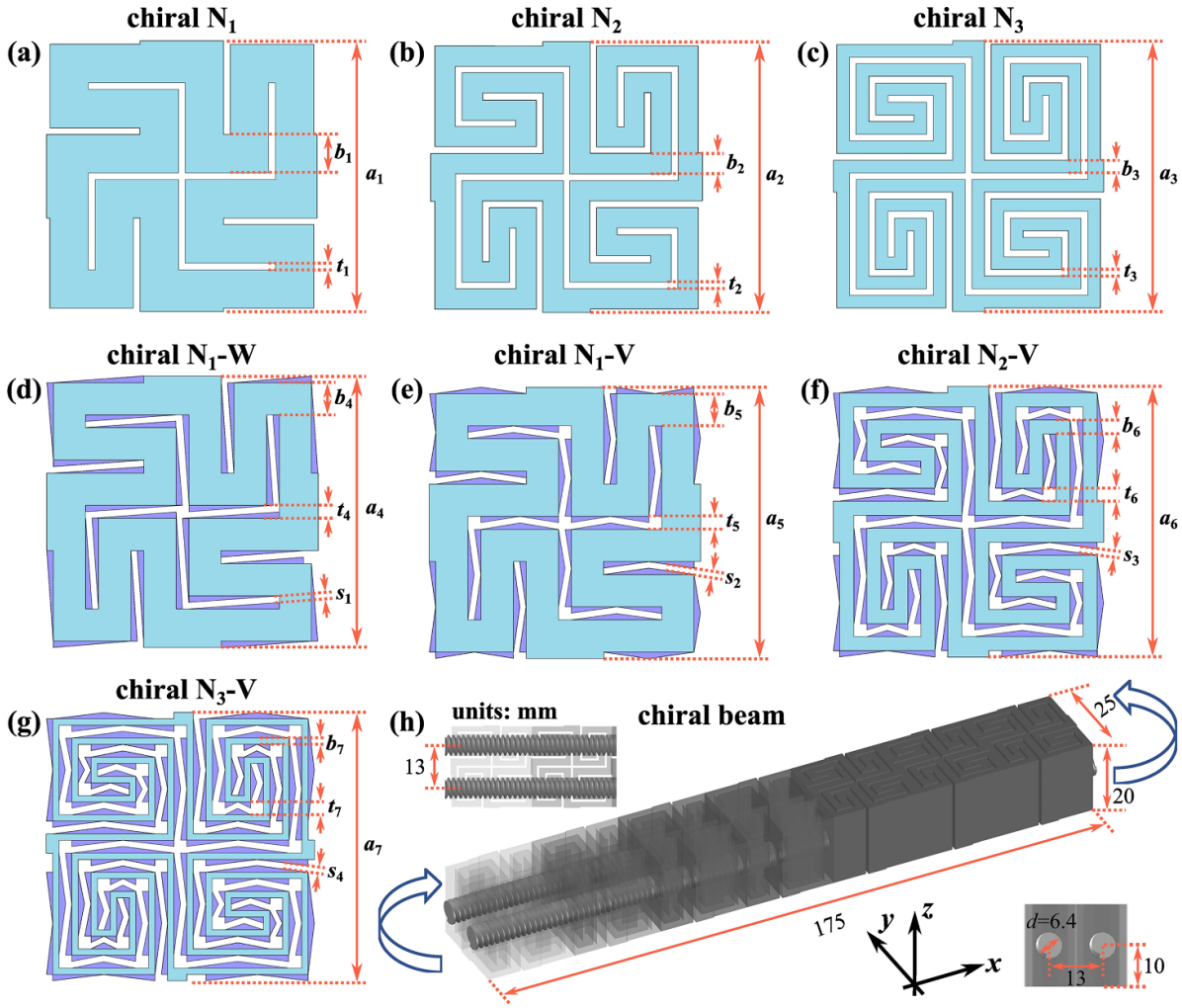


**Figure 1.** Representative chiral unit cells with different orders of structural hierarchy: (a) chiral $N_1$; (b) chiral $N_2$; (c) chiral $N_3$; (d) chiral $N_1$ with wedge-shaped friction elements; (e) chiral $N_1$ with V-shaped friction elements; (f) chiral $N_2$ with V-shaped friction elements; and (g) chiral $N_3$ with V-shaped friction elements, and (h) schematic of the $N_2$ chiral beam specimen with friction rods.

- Chiral-hexagonal (CH) - The CH topology was similar to the CR topology, but adopted a hexagonal hierarchical honeycomb design instead of concentric rectangle. The topology used slits that follow a deterministic center-symmetric geometry to construct a series of concentric open hexagons with progressively decreasing side lengths towards the geometric center. Each hexagon is interconnected or joined to the next hexagon through a shared rib. The CH pattern was characterized by the maximum edge length of the hexagonal lattice $l_5 = 12.80$ mm, varying interior angles $\theta_4 = 130°$, $\theta_5 = 110°$, and $\theta_6 = 120°$, and hexagonal lattice count of 4. These parameters ensured consistency in the overall geometry, rib width, and slit width with the other topologies investigated in this study. The resulting topology is diagrammed in figure 2(e), with a 3D view illustrated in figure 2(f).
- Chiral beams fabrication - Under our investigation, rectangular beams were fabricated using each of the aforementioned topologies, here termed chiral beam specimens. Each chiral beam specimen consisted of 7 repeating chiral unit cell arranged along the longitudinal direction to yield an overall side length $L = 175$ mm, side width $W = 25$ mm, and out-of-plane height $H = 20$ mm, as diagrammed in figure 1(h). The periodic arrangement of the chiral unit cells along the beam is used to create a longitudinal structure, increase energy dissipation through cumulative effects (e.g. more frictional areas), and evenly distribute dissipative forces. Beams were fabricated from polylactic acid (PLA) plastic using a fused deposition modeling (FDM) 3D printer (AnkerMake M5) with a printing resolution of 0.1 mm. The model was sliced using the 3D printing software AnkerMake Studio V0.9.45. 3D printing settings used a nozzle temperature of 210 °C, bed temperature of 70 °C, printing speed of 250 mm $s^{-1}$, layer height of 0.2 mm, wall thickness of 1.24 mm, lines infill patterns, 30% infill ratio, and bottom thickness of 0.1 mm. The bottom thickness was selected to minimize any inadvertent filling of the designed slits due to potential printing resolution errors, preventing the sticking of nearby ribs that would resist rotation. A control beam specimen consisting of a solid geometry of dimensions equal to those of the chiral beam specimens was also printed for benchmarking purposes. Sets of

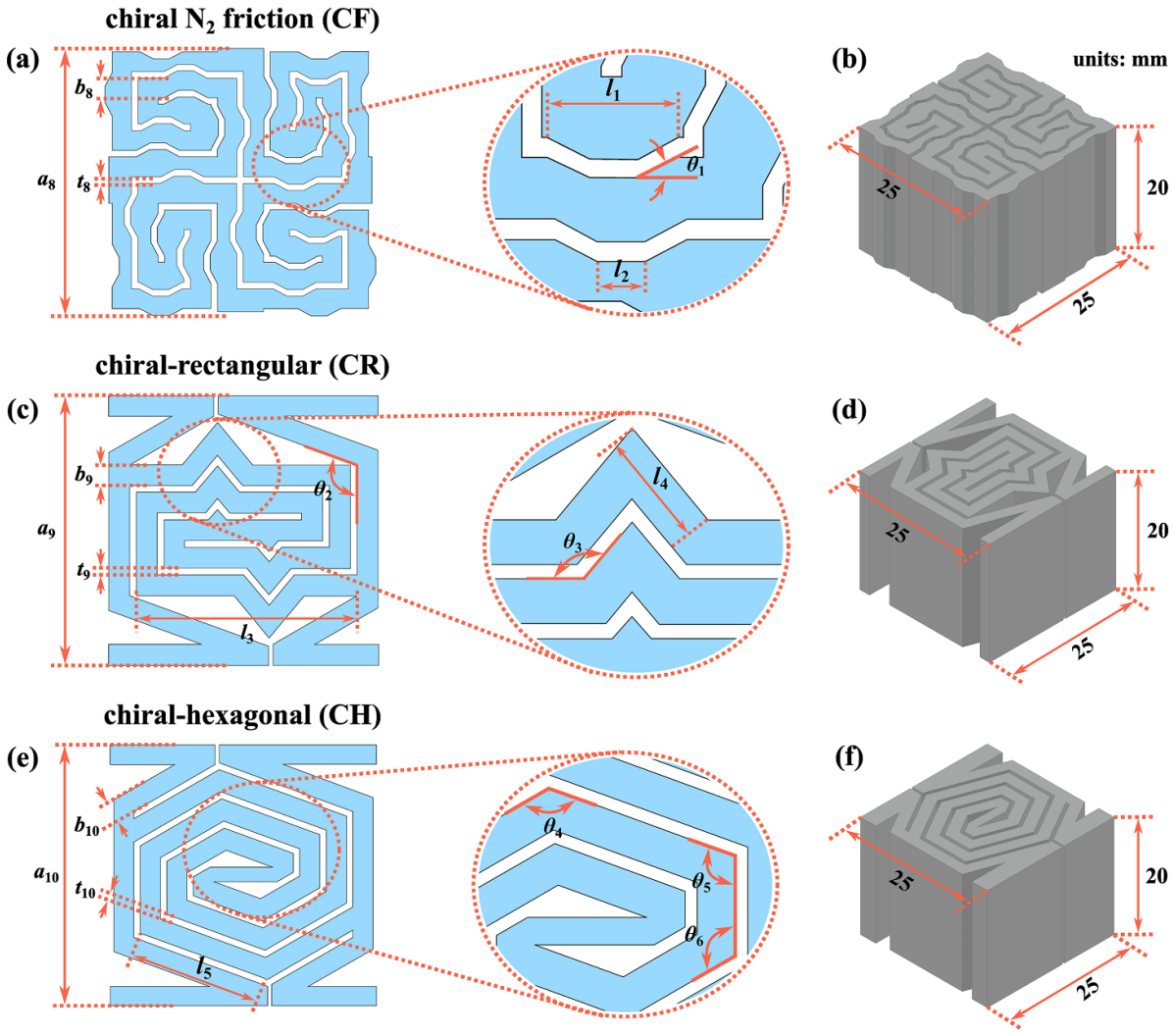


**Figure 2.** Unit cell of the new chiral topologies: (a) chiral $N_2$ friction (CF); (c) chiral-rectangular (CR); and (e) chiral hexagonal (CH).

three specimens were printed under each chiral topologies, for a total of 51 specimens. Remark: results from our investigation present aggregated results obtained from each set of beams, and we thus refer to each metamaterial topology as 'specimen' in the singular form. The interested reader may refer to figures A1–A10 of the appendix to find pictures of each printed chiral beam specimen. The relative density ($\rho$) of each printed chiral beam specimen is tabulated in table 1, which was computed by normalizing the volume with respect to that of the control beam. The raw volumes are table B1 of the appendix.

- Friction rod - Friction rods were designed to be integrated within some of the beam specimens to provide post-fabrication bending stiffness tunability and additional damping through dynamic friction. These friction rods consisted of two 6.35 mm natural nylon threaded rods. The threaded pattern on the nylon rod was used to create contact friction and allow for the controllable post-tensioning mechanisms using rotating hex nuts equipped at each end. Friction rods were inserted through two holes of 6.34 mm diameter positioned 10 mm above the bottom surface and 10 mm apart drilled longitudinally through the entire beam.

## 3. Experimental section

The mechanical properties of specimens in terms of the bending stiffness, midpoint displacement, recoverability, and energy dissipation, were evaluated through a series three-point bending tests. The overall experimental configuration along with the close-up view of the specimen setup are illustrated in figure 6. Tests were performed using a load-controlled universal load frame (Instron 5944, USA) equipped with an 1 kN 2580 series load cell that has a measurement accuracy of $\pm$0.01 mm and 0.05 N. A 2180 series flexure fixture was used to set up the boundary condition of a three-point bending. The chiral beam specimen was horizontally positioned on the supports of the flexure fixture along its longitudinal direction for bending along the $z$-axis, illustrated by the curved arrows in figure 1(h), and was centered on the supports and aligned with

**Table 1.** Physical and mechanical properties for each chiral beam specimen.

| specimen | relative density ($\rho$) (–) | bending stiffness (N mm$^{-1}$) | recovery (%) | $\eta$ (%) | $\widetilde{\eta}$ (%) |
|---|---|---|---|---|---|
| control beam | 1.00 | 196.8 | 99.5 | 0.7 | 0.7 |
| $N_1$ | 0.87 | 7.5 | 98.6 | 1.9 | 2.1 |
| $N_2$ | 0.76 | 2.1 | 96.8 | 3.1 | 4.1 |
| $N_3$ | 0.64 | 0.6 | 88.9 | 2.3 | 3.5 |
| chiral $N_2$ friction (CF) | 0.78 | 1.7 | 96.2 | 3.7 | 4.7 |
| chiral rectangular (CR) | 0.70 | 1.3 | 94.0 | 2.8 | 4.0 |
| chiral hexagonal (CH) | 0.78 | 1.0 | 95.1 | 4.1 | 5.3 |
| $N_1$-W | 0.91 | 9.3 | 98.6 | 2.0 | 2.2 |
| $N_1$-V | 0.92 | 10.3 | 98.3 | 2.3 | 2.6 |
| $N_2$-V | 0.82 | 2.6 | 96.0 | 3.9 | 4.7 |
| $N_3$-V | 0.80 | 1.0 | 92.3 | 3.5 | 4.2 |
| $N_1$+rod | 0.75 | 15.9 | 98.1 | 6.2 | 8.2 |
| $N_2$+rod | 0.66 | 9.0 | 94.6 | 6.8 | 10.4 |
| $N_3$+rod | 0.56 | 5.2 | 97.2 | 3.9 | 6.8 |
| $N_2$-V+rod | 0.71 | 15.6 | 98.7 | 7.2 | 10.1 |
| CH+rod | 0.68 | 16.4 | 94.4 | 8.3 | 12.3 |

the loading point. The support span $S$ was set to 126 mm to comply with the configuration prescribed by ASTM standard D790-17 [46].

The quasi-static tests consisted of a traditional load ramp to characterize specimens' stiffness and strength properties. Tests were performed by applying uniaxial concentric load vertically downward at the mid-point of the specimen through a loading nose. The loading rate was set constant to 0.2 N s$^{-1}$ and stopped until the maximum load reached the prescribed values. The same testing protocol was used for the dynamic tests, during which each specimen was independently subjected to 10 sets of 6-cycle harmonic excitations at 0.1 Hz, with the maximum load magnitudes ranging from 5 N to 50 N in a 5 N increments. The 0.1 Hz frequency selected here was to ensure that the tests captured the material's energy dissipation, bending stiffness variation, and recoverability characteristics under conditions where inertial effects are minimal, which aligns with the quasi-static nature of the study. Load and displacement values were collected at 100 Sample/second, and both the quasi-static and dynamic tests were conducted on sets of three specimens under each topology to investigate the repeatability of results. In some case, identified outliers were removed from the results. An outlier was defined as a result deviating 20% from the three-specimen average, as it is common practice in structural engineering.

## 4. Results and discussion

### 4.1. Bending stiffness

The first functionality of interest was the bending stiffness, which was hypothesized to reduce in order to provide supplemental damping capabilities. The bending stiffness of each specimen was characterized by subjecting beams to a harmonic loading in a three-point bending configuration. The load-displacement curves are presented in figures 3(a)–(f). Displacement measurements were extracted from the testing machine and are equal to the deflection at mid-span. Results show the last cycle from the dynamic test, representing a steady state without transient behavior. A maximum load magnitude of 5 N was assigned to specimens without friction rod to accommodate their higher flexibility caused by a higher fractal order (e.g. $N_3$), and avoid any excessive deflection or local damage/fracture that could occur under a large displacement. The maximum load was increased to 30 N for specimens equipped with friction rods due to their higher stiffnesses in order to explore any potential nonlinear effects under larger deformations.

It was found that the initial chiral topologies resulted in very low stiffnesses and thus larger deflections compared to the control beam (blue line in figure 3(a)). Under constant load, the maximum displacement increased with the increase of the structural hierarchy order. We also observed that the specimens displayed a higher stiffness nonlinearity that increased with an increase in hierarchy order (figure 3(a)), attributable to the larger slit space. A repeatable change in the hysteresis behavior was observed under low displacements ($< 0.5$ mm) on specimens equipped with friction rods, likely attributed to initial slippage of the rod.

The bending stiffness of each specimen was determined through a linear fit of load-displacement curve during loading stage. Given the nonlinear behavior, this stiffness is termed effective bending stiffness. Results are illustrated in figure 3(g). The bar chart shows the three-sample averaged bending stiffness with the error bars indicating the full range of the bending stiffness over the three specimens. Overall, metamaterial beams exhibited a significant decrease

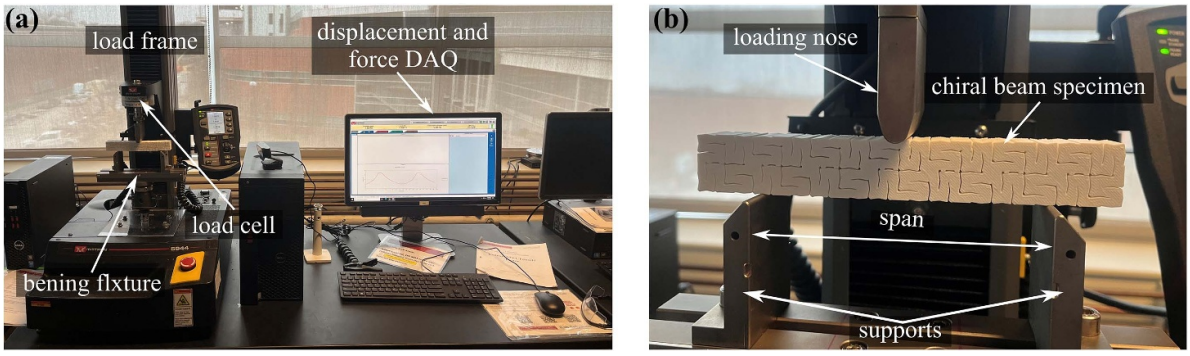


**Figure 3.** Pictures showing (a) experimental configuration; and (b) close-up view of the specimen setup.

in bending stiffness relative to the control beam, as expected. The relative bending decreased with the increasing structural hierarchy order, also attributable to smaller rib thicknesses leading to a smaller relative density and thus smaller moment of inertia. When comparing results across $N_1$ chiral topologies, adding the wedge-shaped and V-shaped friction elements resulted in an average increase of 7.1% and 18.1% in effective bending stiffness, respectively. Equipping specimens with friction rods had significant effect on the effective bending stiffness, increasing it from 112% ($N_1$+rod) to 1538.5% (CH+rod). No plastic deformation or local damage/failure were audible or observable during and after the test, and all specimens, except $N_3$, exhibited at least 90% shape recovery ($R_r$) from the initial un-deformed deflection, where the recovery ratio $R_r$ was computed using the method described in reference [47]:

$$R_r = \frac{d_{max} - d_{res}}{d_{max}} \cdot 100 \tag{2}$$

where $d_{max}$ and $d_{res}$ are the maximum central and residual displacements, respectively. The three-specimen averaged bending stiffness along with the recovery ratio of each chiral beam specimen are listed in table 1. Outliers, here taken as measurements deviating over 20% from the average, were excluded from calculations. We found that adding V-shape friction element and using equipping friction rods can yield lower shape recovery. These lower recovery rates are not necessarily due to inelastic deformations. Instead, they can be attributed to static friction locking the deformation under small motions, which explains slippage observable in the specimens' hysteresis (figure 3(a)). An inspection of the table 1 shows that specimens $N_1$+rod and $N_2$-V+rod were particularly successful at providing higher relative bending stiffness under lower volume density while preserving a high recovery ratio. Specimen CH+rod exhibited the highest stiffness-to-relative density, yet with a low recovery ratio.

### 4.2. Energy dissipation

The second functionality of interest was the supplemental energy dissipation capabilities. To characterize performance, the energy dissipation was computed as the area within the loading-unloading curves in the load-displacement plots (filled areas in figure 3(a)–(f)) [48, 49]. It was anticipated that the viscoelastic properties and friction were the primary energy dissipation mechanisms of the chiral beams investigated in this study, of which the lattice ribs in contact with each other were to dissipate energy via stick-slip friction [50, 51]. The energy dissipated can be observed in figures 3(a) and (d) that plot load-displacement curves obtained from the chiral beam specimens $N_1$, $N_2$, and $N_3$, and $N_1$-V, $N_2$-V, and $N_3$-V, respectively.

We were interested in the energy absorption, taken as the total amount of energy necessary to deform the specimen to a prescribed displacement and is taken as the area beneath the load-displacement curve. It is found that the energy absorption monotonically increased with the increase in structural hierarchy order due to the lower relative stiffness, and that the overall amount of energy dissipated followed a similar trend. We noted that the absorbed energy cannot be transformed entirely into strain energy during the unloading process because of the intrinsic material damping, viscoelastic nature of the based material, elastic buckling, and macro/microscale friction [21]. The loss factor $\eta$ was used to combine these two metrics [52, 53] with:

$$\eta = \frac{\Delta U}{2\pi \cdot U} \cdot 100 \tag{3}$$

where $\Delta U$ is the amount of energy dissipation, $U$ is the amount of energy absorption [52, 53]. A higher loss factor is desirable in characterizing supplemental damping capability. The three-sample averaged loss factors $\eta$ are presented in figure 3(h) with the error bars indicating the full range over the three specimens. We can be observed that: (1) the control beam specimen exhibited poor energy dissipation capability, as expected, with only 4.12% of absorbed energy being dissipated through intrinsic material damping; (2) chiral topologies enabled significantly higher energy dissipation compared to the control beam, resulting in improvements of 411.1% ($N_1$) to 2172.2% (CH+rod) on the loss factor; (3) there was no obvious correlation between the loss factor ($\eta$) and the structural hierarchy order, aligning with the findings reported in [44], likely attributable to the variety of physical mechanisms affecting damping performance; (4) $N_2$ and CH

topologies respectively outperformed in their categories by yielding 66.8% and 27.4% higher loss factor than the $N_1$ and CR topology; (5) incorporating wedge-shaped or V-shaped friction elements enabled additional energy dissipation, over which the V-shape strategy performed better the wedge-shape strategy; (6) the use of V-shaped friction elements resulted in 24.7% ($N_1$-V) to 52.5% ($N_3$-V) higher loss factors than those with the same structural hierarchy orders but without friction elements; (7) the $N_2$-V, CF, and CH topologies resulted in the top three highest loss factors among all topologies without friction rods; (8) the integration of friction rods increased the loss factor of chiral beam specimens by 72.1% ($N_3$-V+rod) to 236.8% ($N_1$+rod) compared to those without the friction rods; and (9) the $N_1$+rod, $N_2$+rod, $N_2$-V+rod, and CH+rod all outperformed in dissipating energy, with the CH+rod significantly outperforming by resulting the highest loss factor of 0.0818, accounting for 52.1% of its energy absorption.

To facilitate a cross-comparison of results with bending stiffnesses, the loss factor $\eta$ is also presented normalized with respect to the relative density of the beams using $\widetilde{\eta} = \eta/\rho$ to provide a performance metric for energy dissipation efficiency in terms of material utilization. The resulting values for the loss factor ($\eta$) and normalized loss factor ($\widetilde{\eta}$) are tabulated in table 1. We observed through $\widetilde{\eta}$ remained that specimens $N_2$+rod, $N_2$-V+rod, and CH+rod exhibited better energy dissipation efficiency. The interested reader with find the amount of energy dissipation and energy absorption obtained from each chiral beam specimen in table B1 of the appendix, and a comparison of the normalized loss factor ($\widetilde{\eta}$)between specimens is in figure C1.

### 4.3. Load-dependence

Another aspect of interest if the load-dependence of specimens in order to investigate scalability. The load-dependence was assessed through a series of additional three-point bending experiments on the $N_2$+rod, $N_2$-V+rod, and CH+rod chiral beam specimens, selected because they exhibited the three highest values in terms of energy dissipation efficiency $\widetilde{\eta}$. Figures 4(a)–(f) plot the load-displacement curves under peak load magnitudes from 5 N to 50 N with a 5 N load increment interval for the selected specimens in three and two dimensions. Pictures showing the maximum central displacement under a 30 N concentrated load are shown in the inset of figures 4(d)–(f). We observed that the $N_2$+rod (figures 4(a) and (d)) and CH+rod (figures 4(c) and (f)) specimens exhibited an approximately linear and constant increase in the loading stage of the load-displacement curves with increasing load. Yet, the loading slope of the $N_2$-V+rod specimen (figures 4(b) and (e)) increased more significantly after reaching a critical central displacement of approximately 4 mm.

Figures 4(g)–(l) are pictures showing the maximum central displacement of the $N_2$ specimen under centrally applied concentrated loads of 0, 10, 20, 30, 50, and returning to 0 N. We noticed that adjacent ribs gradually deviated from a parallel alignment as the maximum central displacement increased, forming angles that open successively from the upper to the lower surface. The largest opening angle formed at mid-span and decreased gradually towards both sides. All tested specimens exhibited an excellent structural integrity without apparent local failure/damage observable or audible during and after the test. The recoverability after unloading slightly decreased when subjecting the specimen to a larger centrally applied concentrated load, likely due to the plastic deformation and fractures at the micro-scale. This behavior is typical for all of the chiral beam specimens tested in this study. Yet, the overall recovery rate of the $N_2$+rod, $N_2$-V+rod, and CH+rod specimens remained in the range of 94.4% to 98.7% under different maximum load magnitudes, forming a complete loading-unloading loop as illustrated in figure 4(d)–(f).

Figure 4(m) compares the three-specimen averaged effective bending stiffness measured from the $N_2$+rod, $N_2$-V+rod, and CH+rod specimens under different maximum loading magnitudes, and the resulting maximum central displacement as a function of loading magnitude are plotted in figure 4(n). The effective bending stiffness of the $N_2$+rod and $N_2$-V+rod specimens was found to be independent of the maximum loading magnitude, where the bending stiffness remained approximately constant under different load magnitudes. However, the CH+rod specimen showed a loss in relative stiffness with the increasing load magnitude. This behavior is also evidenced in figure 4(n).

Figures 4(o)–(q) show the three-specimen mean load-energy absorption, load-energy dissipation, and load-loss factor ($\eta$) for the selected beams. We found that the energy absorption and energy dissipation rates gradually increased with the increasing load for each specimen. However, there is no constant relationship observed for the loss factor across the three specimens. This is due to the fact that energy dissipation and structural damping are affected by different physical mechanisms. The viscoelasticity of the material partially contributes to the energy dissipation, while the energy loss caused by stick-slip friction depends on geometric features and varies with the contact area as the central displacement increases. In the figures, quantity $\eta = 0.06$ is shown as a threshold to allow for a cross-comparison of energy dissipation performance. We can be observed that both the $N_2$-V+rod and CH+rod specimens resulted in higher loss factors compared to the $N_2$+rod specimen when the applied concentrated load exceeded 10 N. The CH+rod specimen exhibited the highest rate of energy dissipation, consistent with the larger area observed within the load-unloading curve displayed in figure 4(f). We also noted that the loss factor $\eta$ of the CH+rod specimen remained approximately consistent for loads beyond 25 N (2.16 mm displacement), but exhibiting a slow decrease in the loss factor towards the 50 N (5.08 mm displacement) load. The interested reader may refer to figure C1 of the appendix for a more detailed comparison of the normalized loss factor ($\widetilde{\eta}$).

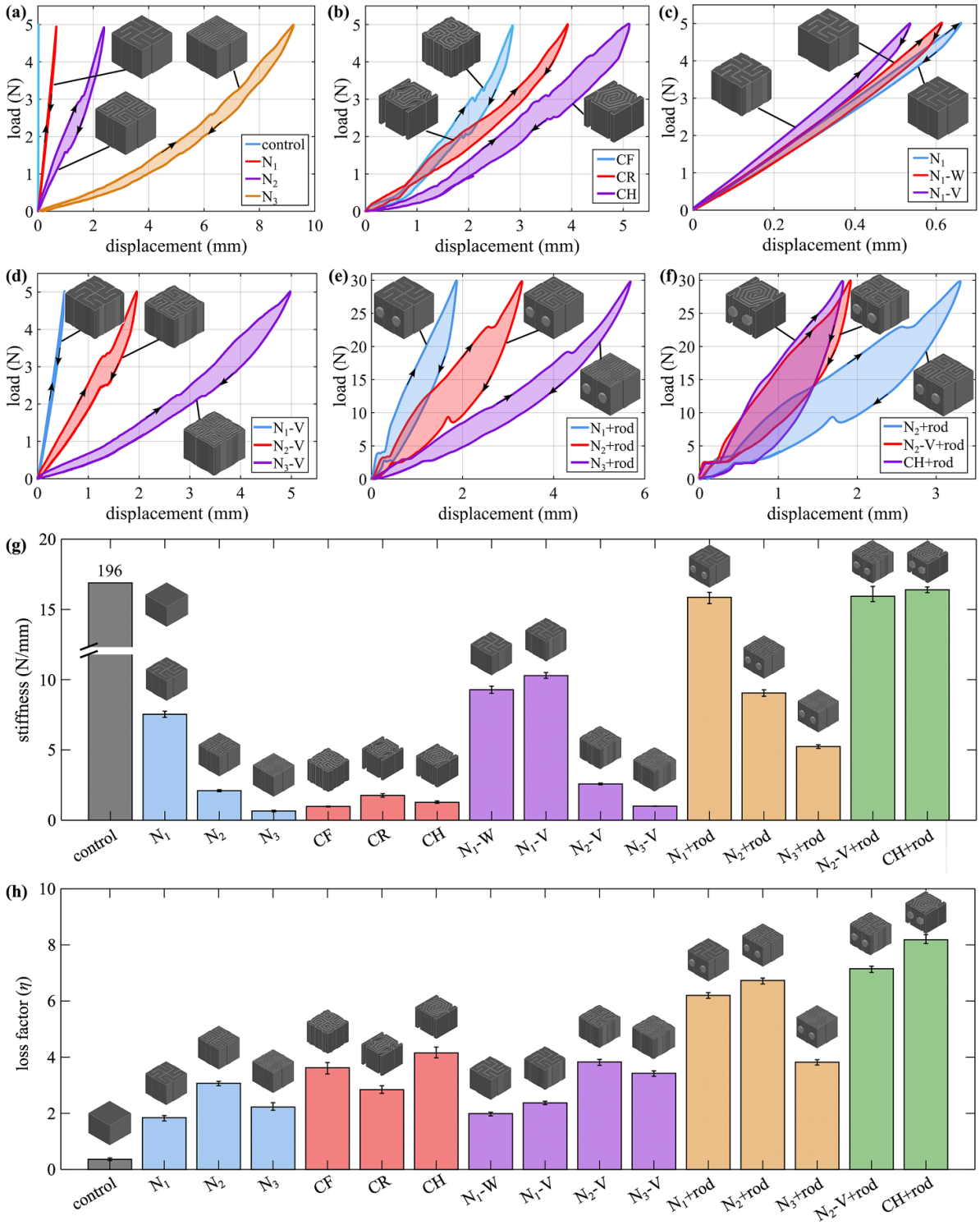


**Figure 4.** Load-displacement curves for: (a)–(c) chiral beams without friction elements; (d) and (f) chiral beams with friction elements and rods, and bar charts comparing (g) the relative bending stiffnesses and (h) loss factors between specimens.

### *4.4. Post-stressing effect*

To explore the effect of post-stressing the friction rod, additional three-point bending experiments were performed on the $N_2$+rod, $N_2$-V+rod, and CH+rod specimens equipped with friction rods. The maximum load magnitude was taken constant at 30 N across all tests. The post-stress varied from 0% to 100%, where 100% corresponds to five full clockwise rotation of the screw nut located at the end of the specimen, with 0% being the nut put in contact with the side wall of the specimen without additional stress. A full rotation of the nut corresponded to a 0.8 mm inward offset. The 100%

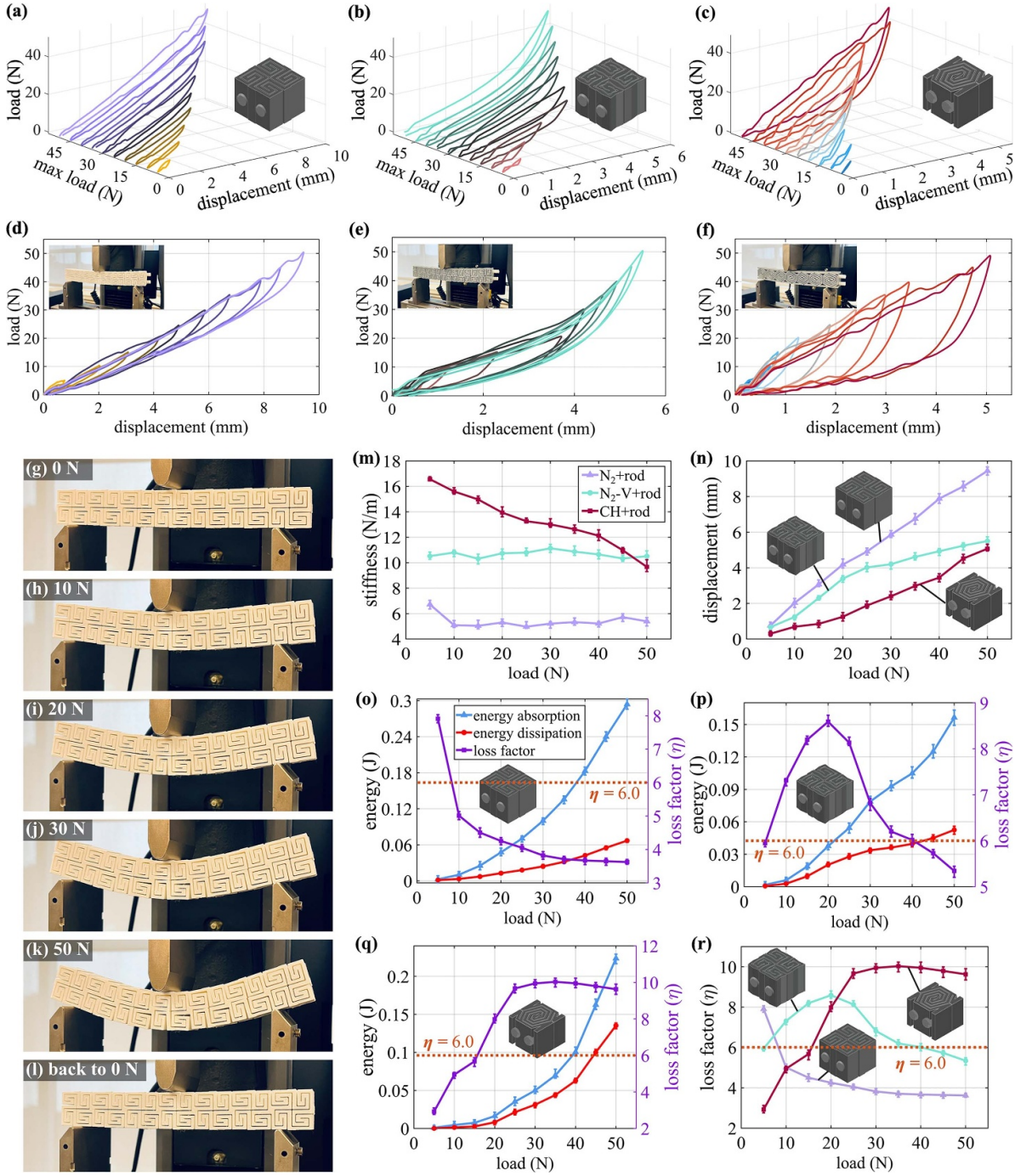


**Figure 5.** Load-displacement curves under different load magnitudes for: (a) CF+rod; (b) CR+rod; (c) CH+rod chiral beam specimens; (d)–(f) 2D views of results plotted in (a)–(c), (g)–(l) pictures showing the bending deformation of the chiral $N_2$ beam specimen under 0, 10, 20, 30, 50, and back to 0 N, (m)–(n) effective bending stiffness and maximum central displacement of CF+rod CR+rod, and CH+rod specimens under different load magnitudes, and (o)–(r) energy dissipation CF+rod, CR+rod, and CH+rod specimens as a function of load mangnitude.

limit was set to prevent local failure/damage. Figures 5(a) to (c) are load-displacement curves measured from the $N_2$+rod (figure 5(a)), $N_2$-V+rod (figure 5(b)), and CH+rod specimens (figure 5(c)). The curves exhibited a similar pattern across all samples, showing higher linearity with the increase in the post-stress level. We also observed that at 100%, the hysteresis is greatly reduced, and the slippage observed under low displacement eliminated.

Figures 5(d)–(f) are pictures showing the maximum central displacement under 40% post-stress. Compared to the $N_2$+rod specimen, an early rib-to-friction element or rib-to-rib contact was observed on the $N_2$-V+rod and the CH+rod specimens,

and the increased surface contact was localized at the joint of the horizontal and vertical ribs because of the geometry. Figures 5(g)–(j) plot the results in terms of the bending stiffness, recovery rate, energy dissipation, and loss factor ($\eta$) for the $N_2$+rod, $N_2$-V+rod, and CH+rod specimens under different post-stressing levels, presenting the mean values from the tested three specimens with error bars indicating the full range of measurements. We observed that the effective bending stiffness (figure 5(g)) monotonically increased with the post-stress level and preserves the bending stiffness ranking. We also confirmed that post-stressing could be used to tune the beam's stiffness, for example allowing the CH+rod beam specimen to reach 90.41 N mm$^{-1}$, equivalent to 47.1% of that of the control beam. Results revealed that configuring a 100% post-stress significantly enhanced the bending stiffness by 668.2%, 938.6%, and 653.1%, and decreased the maximum central displacement by 679.5%, 634.3%, and 937.9% for the $N_2$+rod, $N_2$-V+rod, and CH+rod specimens, respectively.

Figure 5(h) plots the recovery rate versus the post-stress level, depicting an increase in recovery with the increase in the post-stress level. We observed that the recovery rate of all chiral beam specimens reached a recovery rate greater than 99% under a 100% post-stress, with the $N_2$-V+rod specimen yielding the highest ratio (99.29%) with it being remarkably close to that of the control beam (99.46%). This demonstrated that post-stressing can be used as a strategy to tune the recovery rate by serving as a self-centering (e.g. repositioning) mechanism. However, we also observe a trade-off where the tunability of stiffness and recovery rate came at the expense of energy dissipation capabilities, as shown in figure 5(i), where the amount of energy dissipation monotonically decreased with the increase in post-stressing. The resulted loss factors ($\eta$) under each post-stress level are compared in figure 5(j), and the normalized loss factors ($\widetilde{\eta}$) are compared in figure C2 of the appendix. We found that this behavior particularly true for specimen CH+rod that exhibited a considerable gain in both its stiffness and recovery rate with post-stressing, but also a notable decrease in its loss factor. Yet, this trade-off was not as noticeable for the $N_2$+rod specimen that already exhibited a lower loss factor at 0% post-stress. The $N_2$-V+rod specimen yielded the highest loss factor under a post-stress of 20% that subsequently decreased with increasing post-stress, consistent with results obtained under the load-dependence study (figure 4(p)). This is likely attributable to the reduced surface contact between ribs, such that less stick-slip friction can be generated under bending deformation. Nevertheless, we noted that all tested beam specimens under post-stressing yielded a loss factor at least 268.1% higher than that of the control beam, as indicated by the orange dashed line in figure 5(j).

### 4.5. Path to structural applications

Some of the studied specimens showed poor scalability for structural applications, in particular the initial chiral topologies. Yet, through the incorporation of friction elements (wedge- and V-shaped elements), we demonstrated that it was possible to improve energy mitigation while improving bending stiffness relative to the initial topologies. Hence, it may be possible to improve scalability of these topologies through the optimization of their design. Nevertheless, the use of friction rods substantially improved the overall performance both in terms of bending stiffness and energy mitigation capabilities. In particular, specimen CH+rod outperformed all other topologies under both metrics, and did so despite having one of the lowest materials density (68% of the control beam). Its energy dissipation remained approximately stable over larger loads, yet with an observable decrease in performance under the highest load. However, its effective stiffness also decreased under additional loading, while that of specimens $N_2$+rod and $N_2$-V+rod remained approximately constant.

While promising, a critical challenge in the utilization of specimen CH+rod is in its recovery ratio that is significantly lower than that of the other specimens, necessitating pre-cambering and an exact estimation of its bearing load in structural applications. Yet, we also observed that the use of a post-stressing strategy could be used to tune relative bending stiffnesses and energy dissipation capabilities. Particularly for the CH+rod specimen, this tunability represented a trade-off between both performance metrics. Nevertheless, post-stressing resulted in a substantial improvement in its recovery ratio, making it more applicable at larger scales. The $N_2$+rod and $N_2$-V+rod specimens also exhibited some promise under post-stress, with the $N_2$+rod specimen exhibiting an improvement in stiffness and approximately constant loss factor with the increasing level of post-stress, and with the $N_2$-V+rod showing better loss factor than that of the CH+rod under 20% to 80% pre-stress.

Overall, these three specimens ($N_2$+rod, $N_2$-V+rod, and CH+rod) appeared particularly promising at structural applications. We would like to remark that none of our topologies were pre-optimized, and thus their performance could very likely be improved through proper engineering. It is clear, however, that some form of post-stressing mechanism should be included to provided the requisite bending stiffness, while maintaining low material density that could be highly desirable to improve structural sustainability thought materials usage.

The beams under study were fabricated using FDM, a process that constructs components through a layering process. While FDM may be difficult to scale up for larger geometry, mostly due to weak interlayer bonds, FDM-compatible designs are extendable to wire arc additive manufacturing (WAAM) processes, because WAAM forms components through continuous welding along the toolpath [54]. WAAM has been demonstrated at very large scales, including a full-scale pedestrian bridge in Amsterdam [55]. It is therefore hypothesized that our designs under study could be manufactured at much larger scales, but with the understanding that additional research questions will be raised, including whether WAAM can achieve the require resolution to provide sufficient

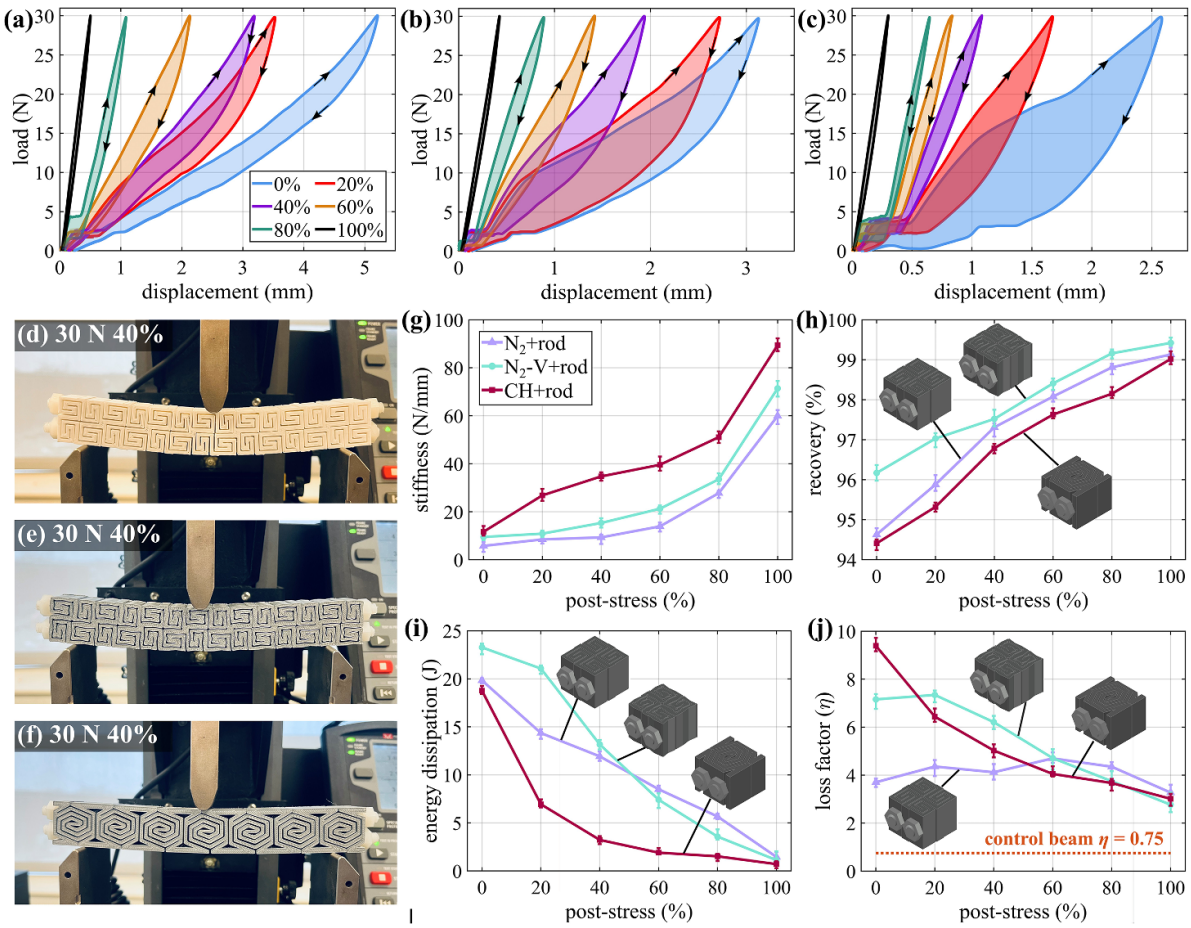


**Figure 6.** Load-displacement curves under different post-stress levels for: (a) CF+rod; (b) CR+rod; and (c) CH+rod specimens, (d)–(f) pictures showing the maximum central displacement yielded on the CF+rod, CR+rod, and CH+rod chiral beam specimens under a concentrated load of 30 N, and (g)–(j) bending stiffness, maximum central displacement, recovery rate, and loss factor as a function of post-stress level for selected specimens.

friction, and how to mitigate the effect of friction wear on 3D printed steel.

## 5. Conclusion

This paper presented a study on scalable metamaterials beams targeting structural engineering applications, for which bending stiffness and supplemental energy dissipation capability are of high interest. The investigated topologies included chiral lattice metamaterials with three orders of structural hierarchy ($N_1$, $N_2$, and $N_3$), with and without elements at the slits to produce Coulomb friction through sliding motion. Three new chiral topologies were also explored namely a chiral friction, a chiral-rectangular, a chiral-hexagonal specimen. Additional frictional effect was introduced by integrating friction rods longitudinally through the middle of the beams that provided additional sliding friction and post-stressing capabilities to tuned the bending stiffness. Beams were 3D printed and their mechanical performance assessed experimentally through a series of three-point bending dynamic tests. Of interest was the bending stiffness, deflection, recoverability, energy absorption, energy dissipation, and loss factors under different maximum loading magnitudes as well as different post-stress levels. The performance of the engineered metamaterial beams was assessed, and a discussion on a path to structural engineering application provided. Experimental results revealed that:

(i) Increasing the fractal order yielded a noticeable decrease in effective bending stiffness.
(ii) The use of friction elements can increase the effective bending stiffness, shape recoverability, energy dissipation ($\eta$). These metrics were improved by 66.6%, 3.8%,

and 52.2%, respectively, by integrating V-shaped friction elements in the $N_3$ specimen.

(iii) Specimens $N_1$+rod, $N_2$-V+rod, and CH+rod exhibited higher relative bending stiffness compared against other metamaterial beams, yet the measured stiffness was significantly lower than that of the control beam.

(iv) Chiral topologies remarkably enhanced energy dissipation compared to the control (solid) beam, up to 11.9 times.

(v) Specimens $N_2$+rod, $N_2$-V+rod, and CH+rod showed high energy dissipation efficiency in terms of materials utilization.

(vi) The use of a non-post-stressed friction rod provided additional energy mitigation and increased relative bending stiffness.

(vii) The loss factors generally varied with the maximum load magnitude applied onto the metamaterial beams, but with no strong correlation was observed.

(viii) The addition of post-stress through the friction rod enabled tuning of the bending stiffness and shape recovery, yet with the trade-off of lowering energy dissipation capabilities.

(ix) Specimens $N_2$+rod, $N_2$-V+rod, and CH+rod appeared particularly promising at structural applications, with specimen CH+rod showing better performance overall.

Results presented in this paper demonstrated the potential in creating scalable metamaterial beams for structural engineering applications. These structural components have the promise of improving structural resilience versus natural hazards (e.g. seismic excitations, high-to-extreme winds) through supplemental damping and reducing embodied carbon by employing less material. It is envisioned that the performance of the studied chiral beams could be optimized to significantly improve the scalability and applicability to structural engineering, including the strategic design of the post-stressable friction mechanism.

## Data availability statement

The data that support the findings of this study are available upon reasonable request from the authors. www.dropbox.com/scl/fo/grtngy8clouegl8u5eikw/AN0h7aW_yBLN6KPHK3z_dUs?rlkey=o1u814jkrzrjiv4u91577k6uj&st=pfylgrng&dl=0.

## Acknowledgments

This material is based upon work supported by the National Science Foundation under Grant No 2349792. Any opinions, findings, and conclusions or recommendations expressed in this material are those of the author(s) and do not necessarily reflect the views of the National Science Foundation. The authors gratefully acknowledge the support of Mr Vedant R Raut from the Department of Civil, Construction and Environmental Engineering at Iowa State University for his assistance with experiments.

## Appendix A. Chiral beam specimens

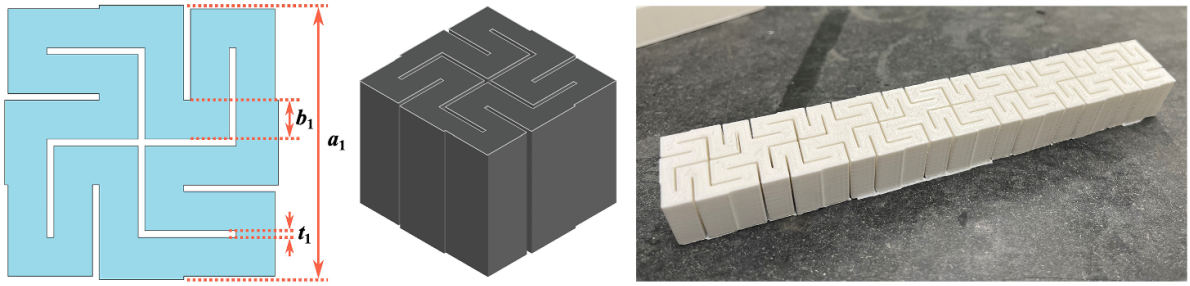


**Figure A1.** Chiral $N_1$ specimen.

**Table A1.** Geometric parameters for the chiral $N_1$ specimen.

| parameter | $a_1$ (mm) | $b_1$ (mm) | $t_1$ (mm) |
|---|---|---|---|
| values | 25 | 3.54 | 0.625 |

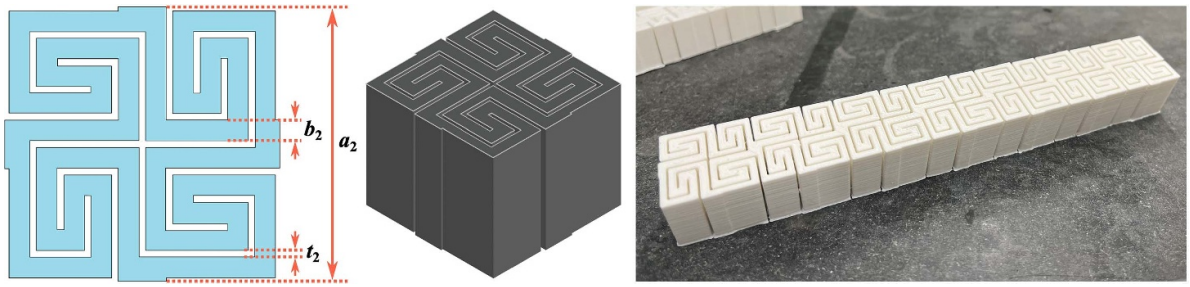


**Figure A2.** Chiral $N_2$ specimen: (left) cross-section; (middle) 3D rendering; and (right) picture.

**Table A2.** Geometric parameters for the chiral $N_2$ specimen.

| parameter | $a_2$ (mm) | $b_2$ (mm) | $t_2$ (mm) |
|---|---|---|---|
| value | 25 | 1.87 | 0.625 |

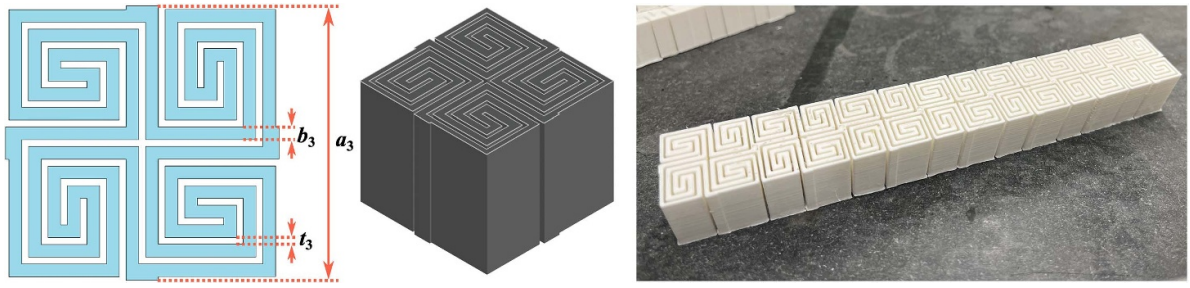


**Figure A3.** Chiral $N_3$ specimen: (left) cross-section; (middle) 3D rendering; and (right) picture.

**Table A3.** Geometric parameters for the chiral $N_3$ specimen.

| parameter | $a_3$ (mm) | $b_3$ (mm) | $t_3$ (mm) |
|---|---|---|---|
| value | 25 | 1.16 | 0.625 |

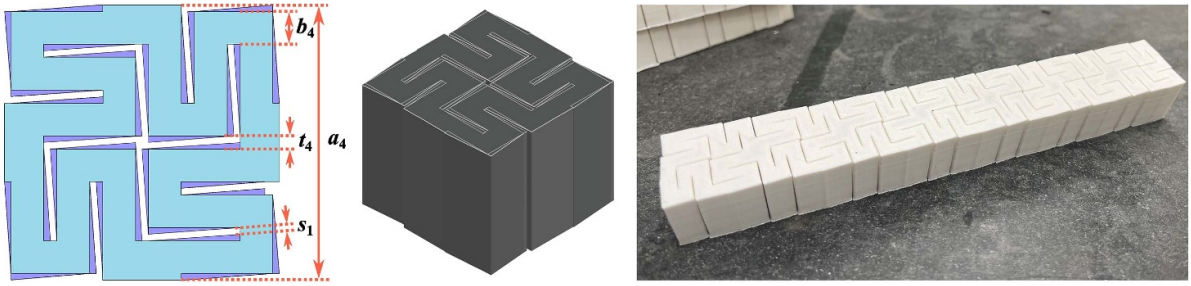


**Figure A4.** Chiral $N_1$-W specimen: (left) cross-section; (middle) 3D rendering; and (right) picture.

**Table A4.** Geometric parameters for the chiral $N_1$-W specimen.

| parameter | $a_4$ (mm) | $b_4$ (mm) | $t_4$ (mm) | $s_1$ (mm) |
|---|---|---|---|---|
| value | 25 | 2.96 | 1.2 | 0.625 |

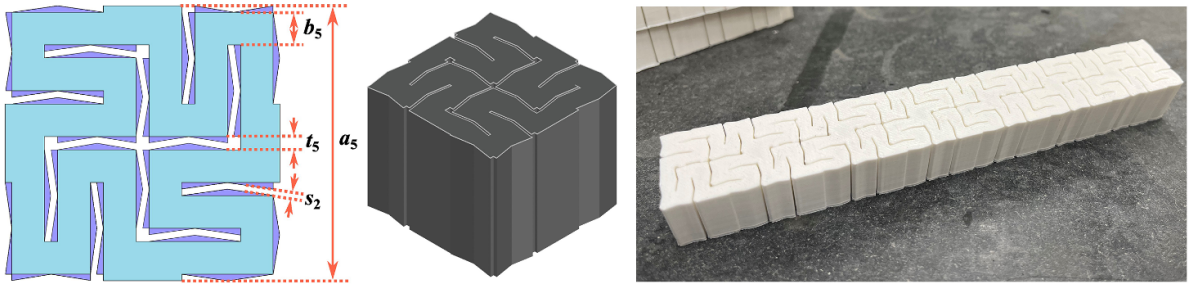


**Figure A5.** Chiral $N_1$ specimen: (left) cross-section; (middle) 3D rendering; and (right) picture.

**Table A5.** Geometric parameters for the chiral $N_1$-V specimen.

| parameter | $a_5$ (mm) | $b_5$ (mm) | $t_5$ (mm) | $s_2$ (mm) |
|---|---|---|---|---|
| value | 25 | 2.96 | 1.2 | 0.625 |

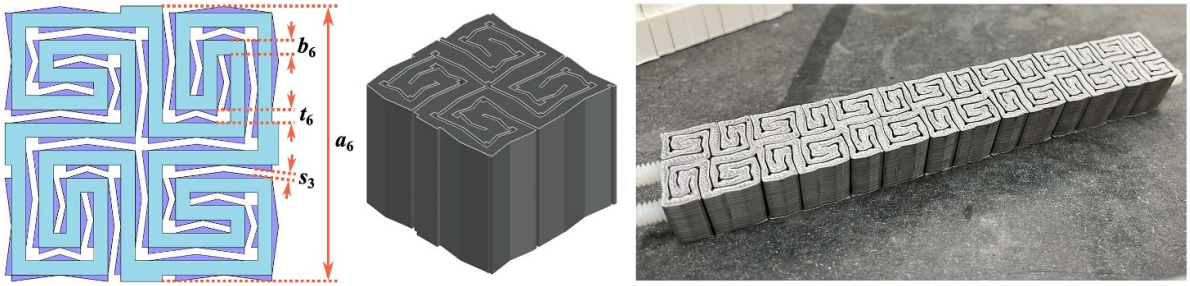


**Figure A6.** Chiral $N_1$ specimen: (left) cross-section; (middle) 3D rendering; and (right) picture.

**Table A6.** Geometric parameters for the chiral $N_2$-V specimen.

| parameter | $a_6$ (mm) | $b_6$ (mm) | $t_6$ (mm) | $s_3$ (mm) |
|---|---|---|---|---|
| value | 25 | 1.3 | 1.2 | 0.625 |

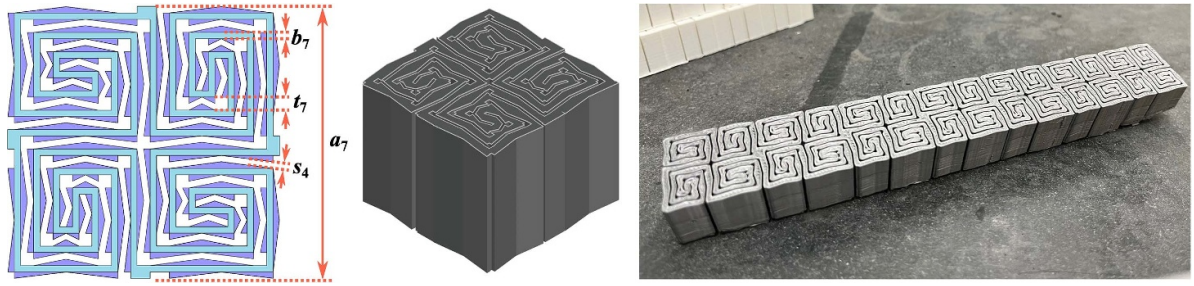


**Figure A7.** Chiral $N_1$ specimen: (left) cross-section; (middle) 3D rendering; and (right) picture.

**Table A7.** Geometric parameters for the chiral $N_3$-V specimen.

| parameter | $a_7$ (mm) | $b_7$ (mm) | $t_7$ (mm) | $s_4$ (mm) | $h$ (mm) | $\theta$ (°) |
|---|---|---|---|---|---|---|
| value | 25 | 0.58 | 1.2 | 0.625 | 7.5 | 5 |

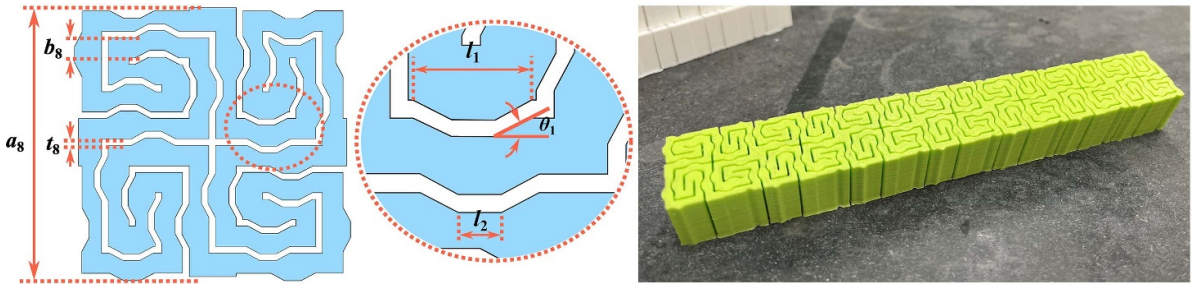


**Figure A8.** Chiral $N_1$ specimen: (left) cross-section; (middle) 3D rendering; and (right) picture.

**Table A8.** Geometric parameters for the chiral friction (CF) specimen.

| parameter | $a_8$ (mm) | $b_8$ (mm) | $t_8$ (mm) | $l_1$ (mm) | $l_2$ (mm) | $\theta_1$ (°) |
|---|---|---|---|---|---|---|
| value | 25 | 1.87 | 0.625 | 1.2 | 0.4 | 30 |

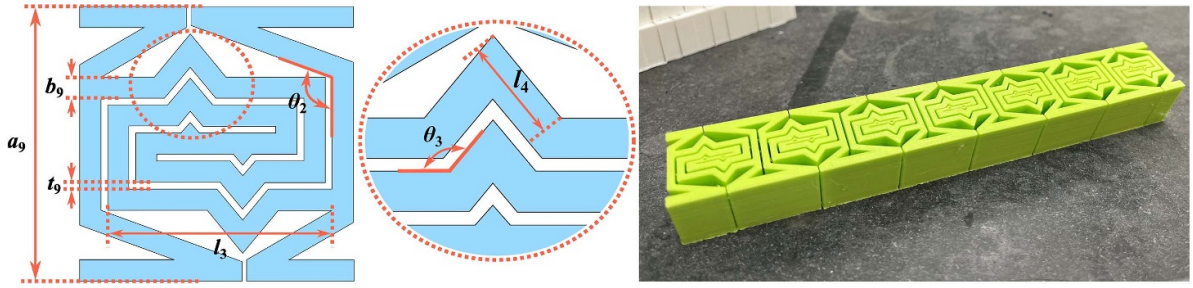


**Figure A9.** Chiral $N_1$ specimen: (left) cross-section; (middle) 3D rendering; and (right) picture.

**Table A9.** Geometric parameters for the chiral rectangular (CR) specimen.

| parameter | $a_9$ (mm) | $b_9$ (mm) | $t_9$ (mm) | $l_3$ (mm) | $l_4$ (mm) | $\theta_2$ (°) | $\theta_3$ (°) |
|---|---|---|---|---|---|---|---|
| value | 25 | 1.87 | 0.625 | 20 | 5 | 110 | 130 |

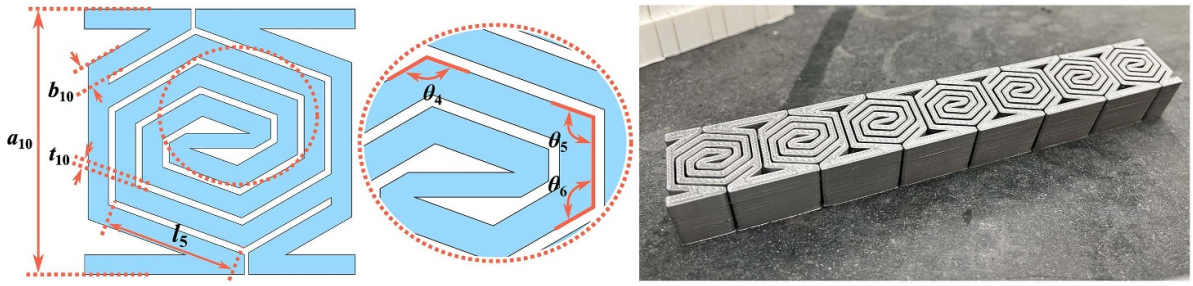


**Figure A10.** Chiral-hexagonal (CH) specimen: (left) cross-section; (middle) 3D rendering; and (right) picture.

**Table A10.** Geometric parameters for the chiral-hexagonal (CH) specimen.

| parameter | $a_{10}$ (mm) | $b_{10}$ (mm) | $t_{10}$ (mm) | $l_5$ (mm) | $\theta_4$ (°) | $\theta_5$ (°) | $\theta_6$ (°) |
|---|---|---|---|---|---|---|---|
| value | 25 | 1.87 | 0.625 | 12.8 | 130 | 110 | 120 |

## Appendix B. Energy metric

**Table B1.** Physical and mechanical properties characterized from each chiral beam specimen.

| specimen | volume (mm$^3$) | energy absorption ($U$) ($J$) | energy dissipation ($\Delta U$) ($J$) |
|---|---|---|---|
| control beam | 87 500 | 0.2171 | 0.0102 |
| $N_1$ | 76 051 | 1.6326 | 0.1926 |
| $N_2$ | 66 280 | 6.3156 | 1.2279 |
| $N_3$ | 56 392 | 26.9409 | 3.8625 |
| $N_2$ friction (CF) | 68 172 | 7.5534 | 1.7375 |
| rectangular (CR) | 60 940 | 11.6296 | 2.0337 |
| hexagonal (CH) | 67 889 | 14.9907 | 3.8736 |
| $N_1$-W | 79 990 | 0.8926 | 0.1135 |
| $N_1$-V | 79 596 | 0.8479 | 0.1241 |
| $N_2$-V | 71 940 | 5.2461 | 1.2709 |
| $N_3$-V | 72 064 | 12.2879 | 2.6604 |
| $N_1$+rod | 66 146 | 28.7927 | 11.2435 |
| $N_2$+rod | 57 279 | 56.1654 | 23.9039 |
| $N_3$+rod | 48 843 | 92.9588 | 22.3547 |
| $N_2$-V+rod | 62 381 | 30.7829 | 13.8980 |
| CH+rod | 59 521 | 28.2817 | 14.8675 |

## Appendix C. Normalized Loss Factor

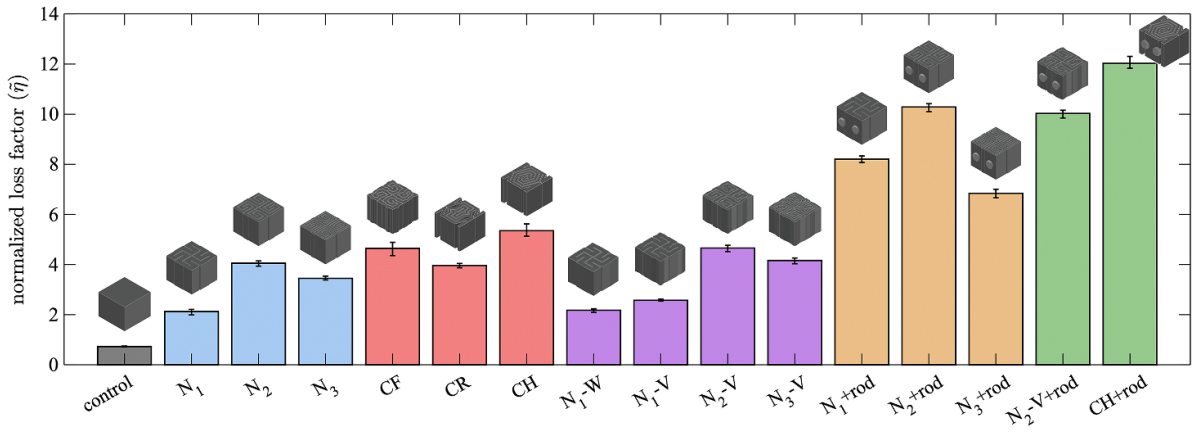


**Figure C1.** Bar charts comparing normalized loss factors ($\widetilde{\eta}$) between specimens.

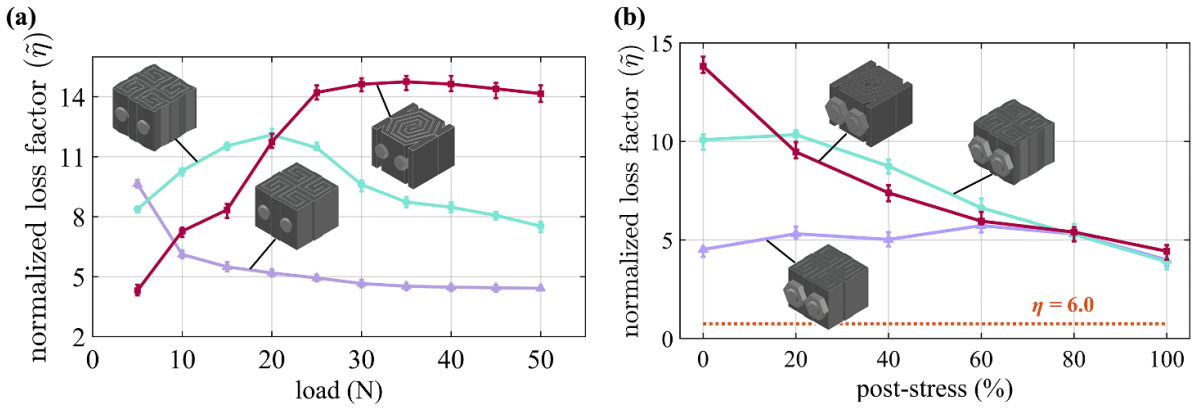


**Figure C2.** Normalized loss factor ($\tilde{\eta}$) as a function of (a) load magnitude; and (b) post-stress level for selected specimens.

## ORCID iDs

Han Liu https://orcid.org/0000-0003-3057-522X
Simon Laflamme https://orcid.org/0000-0002-0601-9664

## References

[1] White B C, Garland A, Alberdi R and Boyce B L 2021 Interpenetrating lattices with enhanced mechanical functionality *Addit. Manuf.* **38** 101741
[2] Lakes R S 2001 Extreme damping in composite materials with a negative stiffness phase *Phys. Rev. Lett.* **86** 2897–900
[3] Pyo S and Park K 2023 Mechanical metamaterials for sensor and actuator applications *Int. J. Precis. Eng. Manuf. Green Technol.* **11** 291–320
[4] Lin Y-S and Xu. Z 2020 Reconfigurable metamaterials for optoelectronic applications *Int. J. Optomechatronics* **14** 78–93
[5] Smith D R, Pendry J B and Wiltshire M C K 2004 Metamaterials and negative refractive index *Science* **305** 788–92
[6] Muhammad and Lim C W 2021 From photonic crystals to seismic metamaterials: a review via phononic crystals and acoustic metamaterials *Arch. Comput. Methods Eng.* **29** 1137–98
[7] Dai H, Zhang X, Zheng Y, Pei W, Zhou R, Liu R and Gong Y 2022 Review and prospects of metamaterials used to control elastic waves and vibrations *Front. Phys.* **10** 1069454
[8] Kumar R, Kumar M, Singh Chohan J and Kumar S 2022 Overview on metamaterial: history, types and applications *Mater. Today: Proc.* **56** 3016–24
[9] Kappe K, Wahl J P, Gutmann F, Boyadzhieva S M, Hoschke K and Fischer S C L 2022 Design and manufacturing of a metal-based mechanical metamaterial with tunable damping properties *Materials* **15** 5644
[10] Kathryn Thompson M *et al* 2016 Design for additive manufacturing: trends, opportunities, considerations and constraints *CIRP Ann.* **65** 737–60
[11] Askari M *et al* 2020 Additive manufacturing of metamaterials: a review *Addit. Manuf.* **36** 101562
[12] Fan J, Zhang L, Wei S, Zhang Z, Choi S-K, Song B and Shi Y 2021 A review of additive manufacturing of metamaterials and developing trends *Mater. Today* **50** 303–28
[13] Lee J-H, Singer J P and Thomas E L 2012 Micro/nanostructured mechanical metamaterials *Adv. Mater.* **24** 4782–810
[14] Christensen J, Kadic M, Wegener M, Kraft O and Wegener M 2015 Vibrant times for mechanical metamaterials *MRS Commun.* **5** 453–62
[15] Zhang X, Wang Y, Ding B and Li. X 2019 Design, fabrication and mechanics of 3D micro-/nanolattices *Small* **16** 1902842
[16] Chen Y, Li T, Scarpa F and Wang L 2017 Lattice metamaterials with mechanically tunable poisson's ratio for vibration control *Phys. Rev. Appl.* **7** 024012
[17] Jia Z, Liu F, Jiang X and Wang L 2020 Engineering lattice metamaterials for extreme property, programmability and multifunctionality *J. Appl. Phys.* **127** 150901
[18] Fernandes M C, Aizenberg J, Weaver J C and Bertoldi K 2020 Mechanically robust lattices inspired by deep-sea glass sponges *Nat. Mater.* **20** 237–41
[19] Wu W, Hu W, Qian G, Liao H, Xu X and Berto F 2019 Mechanical design and multifunctional applications of chiral mechanical metamaterials: a review *Mater. Des.* **180** 107950
[20] Valipour A, Kargozarfard M H, Rakhshi M, Yaghootian A and Sedighi H M 2021 Metamaterials and their applications: an overview *Proc. Inst. Mech. Eng.* L **236** 2171–210
[21] Salari-Sharif L, Schaedler T A and Valdevit L 2014 Energy dissipation mechanisms in hollow metallic microlattices *J. Mater. Res.* **29** 1755–70
[22] Deng H, Cheng L, Liang X, Hayduke D and To A C 2020 Topology optimization for energy dissipation design of lattice structures through snap-through behavior *Comput. Methods Appl. Mech. Eng.* **358** 112641
[23] Zhang Y, Tichem M and van Keulen F 2021 A novel design of multi-stable metastructures for energy dissipation *Mater. Des.* **212** 110234
[24] Garland A P *et al* 2020 Coulombic friction in metamaterials to dissipate mechanical energy *Extreme Mech. Lett.* **40** 100847
[25] Maskery I, Aboulkhair N T, Aremu A O, Tuck C J, Ashcroft I A, Wildman R D and Hague R J M 2016 A mechanical property evaluation of graded density Al-Si10-Mg lattice structures manufactured by selective laser melting *Mater. Sci. Eng.* A **670** 264–74
[26] Mueller J and Shea K 2018 Stepwise graded struts for maximizing energy absorption in lattices *Extreme Mech. Lett.* **25** 7–15
[27] Al-Saedi D S J, Masood S H, Faizan-Ur-Rab M, Alomarah A and Ponnusamy P 2018 Mechanical properties and energy absorption capability of functionally graded f2bcc lattice fabricated by slm *Mater. Des.* **144** 32–44
[28] Jin N, Wang F, Wang Y, Zhang B, Cheng H and Zhang H 2019 Failure and energy absorption characteristics of four lattice structures under dynamic loading *Mater. Des.* **169** 107655

[29] Ghareeb A and Elbanna A 2019 Extreme enhancement of interfacial adhesion by bulk patterning of sacrificial cuts *Extreme Mech. Lett.* **28** 22–30
[30] Siegmund T, Barthelat F, Cipra R, Habtour E and Riddick J 2016 Manufacture and mechanics of topologically interlocked material assemblies *Appl. Mech. Rev.* **68** 040803
[31] Wang Q, Li Z, Zhang Y, Cui S, Yang Z and Lu Z 2020 Ultra-low density architectured metamaterial with superior mechanical properties and energy absorption capability *Composites* B **202** 108379
[32] Prall D and Lakes R S 1997 Properties of a chiral honeycomb with a poisson's ratio of - 1 *Int. J. Mech. Sci.* **39** 305–14
[33] Grima J N, Gatt R and Farrugia P-S 2008 On the properties of auxetic meta-tetrachiral structures *Phys. Status Solidi* b **245** 511–20
[34] Ye H-M *et al* 2010 Surface stress effects on the bending direction and twisting chirality of lamellar crystals of chiral polymer *Macromolecules* **43** 5762–70
[35] Wang J-S, Wang G, Feng Xi-Q, Kitamura T, Kang Y-L, Yu S-W and Qin Q-H 2013 Hierarchical chirality transfer in the growth of towel gourd tendrils *Sci. Rep.* **3** 3102
[36] Wu W, Qi D, Liao H, Qian G, Geng L, Niu Y and Liang J 2018 Deformation mechanism of innovative 3D chiral metamaterials *Sci. Rep.* **8** 12575
[37] Cummer S A, Christensen J and Alú A 2016 Controlling sound with acoustic metamaterials *Nat. Rev. Mater.* **1** 16001
[38] Gao N, Zhang Z, Deng J, Guo X, Cheng B Hou H Cheng Baozhu and Hou Hong 2022 Acoustic metamaterials for noise reduction: a review *Adv. Mater. Technol.* **7** 2100698
[39] Zhu W, Deng W, Liu Y, Lu J, Wang H-X, Lin Z-K, Huang X, Jiang J-H and Liu Z 2023 Topological phononic metamaterials *Rep. Prog. Phys.* **86** 106501
[40] Saha D, Glanville P and Karpov E G 2020 Analysis of antichiral thermomechanical metamaterials with continuous negative thermal expansion properties *Materials* **13** 2139
[41] Ye M, Gao L, Wang F and Li. H 2021 A novel design method for energy absorption property of chiral mechanical metamaterials *Materials* **14** 5386
[42] Li Y and Zhang H 2022 Band gap mechanism and vibration attenuation characteristics of the quasi-one-dimensional tetra-chiral metamaterial *Eur. J. Mech.* A **92** 104478
[43] Zhang W, Neville R, Zhang D, Scarpa F, Wang L and Lakes R 2018 The two-dimensional elasticity of a chiral hinge lattice metamaterial *Int. J. Solids Struct.* **141–142** 254–63
[44] Zhang Z, Scarpa F, Bednarcyk B A and Chen Y 2021 Harnessing fractal cuts to design robust lattice metamaterials for energy dissipation *Addit. Manuf.* **46** 102126
[45] Connor J and Laflamme S 2014 *Structural Motion Engineering* (Springer)
[46] ASTM 2017 D790 - flexural properties of unreinforced and reinforced plastics and electrical insulating materials *ASTM Stand.* **08.01** 12
[47] Zhao Q, Jerry Qi H and Xie T 2015 Recent progress in shape memory polymer: new behavior, enabling materials and mechanistic understanding *Prog. Polym. Sci.* **49–50** 79–120
[48] Bauer J, Meza L R, Schaedler T A, Schwaiger R, Zheng X and Valdevit L 2017 Nanolattices: an emerging class of mechanical metamaterials *Adv. Mater.* **29** 1701850
[49] Luna Vera O S, Kim C W and Oshima Y 2017 Energy dissipation and absorption capacity influence on experimental modal parameters of a pc girder *J. Phys.: Conf. Ser.* **842** 012038
[50] Han L, Yin J, Wang L, Chia K-K, Cohen R E, Rubner M F, Ortiz C and Boyce M C 2012 Tunable stimulus-responsive friction mechanisms of polyelectrolyte films and tube forests *Soft Matter* **8** 8642
[51] Pandya N S, Shah H, Molana M and Kumar Tiwari A 2020 Heat transfer enhancement with nanofluids in plate heat exchangers: a comprehensive review *Eur. J. Mech.* B **81** 173–90
[52] Orban F 2011 Damping of materials and members in structures *J. Phys.: Conf. Ser.* **268** 012022
[53] Treviso A, Van Genechten B, Mundo D and Tournour M 2015 Damping in composite materials: properties and models *Composites* B **78** 144–52
[54] Li J Z, Rizal Alkahari M, Ana Binti Rosli N, Hasan R, Nizam Sudin M and Redza Ramli F 2019 Review of wire arc additive manufacturing for 3d metal printing *Int. J. Autom. Technol.* **13** 346–53
[55] Gardner L, Kyvelou P, Herbert G and Buchanan C 2020 Testing and initial verification of the world's first metal 3d printed bridge *J. Constr. Steel Res.* **172** 106233